

On the time integration for phase field modeling of grain growth in additive manufacturing

Chaoqian Yuan^a, Chinnapat Panwisawas^b, Ye Lu^{a,*}

^a*Department of Mechanical Engineering, University of Maryland Baltimore County, Baltimore, USA*

^b*School of Engineering and Materials Science, Queen Mary University of London, London E1 4NS, UK*

Abstract

Phase field simulations play a key role in the understanding of microstructure evolution in additive manufacturing. However, they have been found extremely computationally expensive. One of the reasons is the small time step requirement to resolve the complex microstructure evolution during the rapid solidification process. This paper investigates the possibility of using a class of stabilized time integration algorithms to accelerate such phase field simulations by increasing the time steps. The specific time integration formulation and theoretical analysis on energy stability were developed, based on a phase field model dedicated to simulating rapid solidification in additive manufacturing. The numerical results confirmed that the proposed method can ensure the numerical stability and a decreasing energy requirement for the phase field simulations with at least two orders-of-magnitude larger time steps over conventional explicit methods. 2D and 3D phase field simulations have been conducted with relevant physical and kinetic parameters for 316L stainless steels. This work provides a numerical framework for efficient phase field simulations and open numerous opportunities for large scale phase field modeling.

Keywords: Additive manufacturing, Phase field simulation, Stabilized semi-implicit scheme, Microstructure evolution, Rapid solidification

1. Introduction

Additive manufacturing (AM) is a promising manufacturing technology for producing complex parts with high design flexibility and minimal material waste [1, 2, 3, 4, 5, 6]. With appropriate post-processing treatments, 3D printed parts have been shown to match or even surpass the performance of conventionally manufactured counterparts [7]. However, the complex thermal cycles, including the rapid heating and cooling rates, involved in the printing processes (e.g., laser powder bed fusion) often lead to complex heterogeneous microstructures in printed materials [8]. In addition, numerous studies have shown that process parameters, including heat source power, scanning speed, and scanning strategy, have a significant influence on microstructure evolution and the resulting mechanical properties [9, 10, 11, 12, 13, 14]. Therefore, understanding the microstructure evolution and their relationship to process parameters is crucial for improving the quality and performance of parts produced by AM processes.

Numerical simulations have been developed to understand the microstructure evolution in AM processes. They are usually based on numerical models developed for solidification processes [15]. Three approaches can be used, including cellular automata (CA) [16, 17, 18, 19, 20], kinetic Monte Carlo (KMC) method [21, 22, 23, 24, 25] and phase field method (PFM) [26, 27, 28, 29, 30, 31]. Compared to PFM, the primary advantage of CA and KMC methods lies in their relatively low computational cost, which enables large volume simulations for understanding the overall texture development in 3D printed materials. They can capture several key features of AM microstructure, like the epitaxial growth of columnar grains. However, their rule-based framework may limit the generalizability. For example, the traditional CA model developed by Gandin and Rappaz employs stochastic rules to represent dendritic growth

*Corresponding author

Email address: ye.lu@umbc.edu (Ye Lu)

[32, 33, 16], which might be difficult to capture the planar transition of the solid–liquid interface during the increase of interfacial velocity [34]. In the KMC approach [22, 23, 25], due to the lack of continuous field representation, the coupling with complex thermal and mechanical fields may be difficult. The PFM is regarded as a more accurate approach for simulating microstructure evolution, as it is derived from irreversible thermodynamics and provides a natural framework for incorporating driving forces of different nature. Nevertheless, due to the high computational expenses of the PFM, the simulations are often limited to 2D cases or small volumes with simplified physical assumptions [35, 36, 37, 29, 30]. Therefore, accelerating phase field simulations is crucial to enlarge the computational domain, incorporate multiphysics coupling effects, and validate the numerical models with experimental samples.

Various techniques have been developed to accelerate phase field simulations by reducing the computational complexity in the PFM or constructing surrogate models. These include adaptive meshing [38, 39, 40], high order approximation methods [41, 42], data and physics-informed machine learning [43, 44, 45, 46, 47, 48], data-based model reduction [49, 50, 51], and more recently, data-free tensor decomposition technique [52]. Another important aspect to consider is to reduce the cost for time integration. In spite of the various time integration schemes for related problems [53, 54, 55, 56, 57, 58, 59], explicit type schemes are still popular for actual phase field simulations of AM microstructure [60, 46], due to their simplicity and the ease of implementation. However, it is known that explicit schemes could require very small time steps due to the stability concerns, leading to a large number of time increments when a realist time scale is considered for AM simulations. To the best of our knowledge, very little work has been reported on the use of alternative implicit or semi-implicit schemes for phase field simulations in AM, partially due to the complexity of the models and the potential physical constraints imposed by the rapid cool rates in AM.

In this work, we studied the feasibility of alternative time integration algorithms, especially a class of stabilized semi-implicit schemes, originally developed for the Allen-Cahn equation with constant coefficients and a relatively simple energy definition [53]. For actual phase field simulations of AM microstructure evolution, several difficulties have to be considered carefully. For example, the phase field variable becomes multi-phase fields, a specific formulation needs to be derived for each phase field variable with appropriate stability conditions. The free energy defined for AM phase field models (e.g., [30]) usually involves multi-source terms that couple several driving forces of different nature, which is non-convex and may cause numerical stability issues. The coefficient of equation (e.g., mobility) is not constant at the solid-liquid interface. To address these challenges, we develop the specific stabilized semi-implicit formulation with an appropriate stabilization coefficient suitable for AM phase field models, with a revisited discrete energy law. We used a phase field model [30] specially designed for rapid solidification in AM processes as an example to illustrate our development. 2D and 3D phase field simulations have been conducted using the relevant physical and kinetic parameters for AM 316L stainless steels. It is found that the proposed method can enable two orders-of-magnitude larger time steps than a traditional explicit scheme, without violating the energy stability requirement. And the solutions are found accurate and can reproduce the key observations from experiments [31] regarding different scan speeds and kinetic anisotropy effects.

This paper is organized as follows. Section 2 presents the theory of the phase field model and the key assumptions and a finite element formulation. Section 3 presents the proposed time integration and the revisited discrete energy law and the energy stability analysis. Section 4 presents some 2D and 3D numerical experiments using the proposed method. Finally, the paper closes with some concluding remarks.

2. Problem formulation

2.1. Model assumptions

The present phase field model was developed under the following assumptions [30].

- The model is considered for a binary Fe–Cr alloy system, using a relatively large effective equilibrium distribution coefficient for austenite, and solute segregation is expected to be small.
- The model considers solidification near the limit of absolute stability, where solute trapping becomes significant. Under these conditions, the solidification is expected to proceed predominantly with either planar interfaces or low-amplitude cells [30, 34], which is consistent with theoretical calculations of interfacial velocity for 316L stainless steel under rapid solidification conditions [61].

- It is assumed that grains grow exclusively via epitaxial growth from pre-existing grains, with no new grain nucleation occurring during the process.
- The model assumes that the solid-liquid interfacial energy is isotropic, neglecting any orientation dependency of the interfacial energy.
- The kinetic anisotropy is incorporated, by assuming that the solid-liquid interface velocity is strongly dependent on crystallographic orientation, i.e., interface mobility varies significantly with different crystal planes. This anisotropy plays a crucial role in competitive grain growth and morphological evolution during rapid solidification.

2.2. Phase field model of grain growth

In this model, the order parameter (OP) denotes the grains with the same crystal orientation. The governing equation for the evolution of each OP in the phase field model is given by the gradient flow equation [62]

$$\frac{\partial \phi_i}{\partial t} = M_i \frac{\delta E}{\delta \phi_i}, \quad (1)$$

where ϕ_i is the i th order parameter, M_i is the mobility of the i th phase, and E is the total free energy. The evolution is driven by the total free energy which usually includes a bulk potential and a gradient energy term to account for phase stability and interfacial effects, respectively

$$E = \int_{\Omega} \mathcal{F}(\{\phi\}, \{\nabla \phi\}) d\Omega = \int_{\Omega} \left[f(\{\phi\}, T) + \frac{\kappa}{2} \sum_{i=0}^N |\nabla \phi_i|^2 \right] d\Omega, \quad (2)$$

where $\{\phi\}$ is the set of all ϕ_i , $\{\nabla \phi\}$ is the set of all $\nabla \phi_i$, $f(\{\phi\}, T)$ is the homogeneous free energy, and κ is the gradient energy coefficient. The parameter κ is related to the interfacial width in the phase-field model, although it is not directly equal to it. A more precise definition will be provided in the following sections. The gradient flow equation is expressed in terms of a functional derivative. To facilitate numerical solution, we reformulate the governing equation as a partial differential equation by deriving its variational form. To derive the variational form of Eq.(1), we consider a perturbation of the order parameter ϕ_i in the direction of a smooth function η , and examine the first variation of the energy functional E . Here, η is assumed to be a sufficiently smooth function with compact support in Ω , i.e., $\eta \in C^\infty(\Omega)$, or more generally, $\eta \in H_0^1(\Omega)$ if weak formulations are considered. This ensures that η vanishes on the boundary. Therefore, we apply Eq.(2) to Eq.(1)

$$\begin{aligned} \int_{\Omega} \frac{\delta E}{\delta \phi_i} \eta d\Omega &= \int_{\Omega} \lim_{\epsilon \rightarrow 0} \frac{\mathcal{F}(\phi_i + \epsilon \eta, \nabla \phi_i + \epsilon \nabla \eta) - \mathcal{F}(\phi_i, \nabla \phi_i)}{\epsilon} d\Omega \\ &= \int_{\Omega} \frac{\partial \mathcal{F}}{\partial \phi_i} \eta + \frac{\partial \mathcal{F}}{\partial \nabla \phi_i} \nabla \eta d\Omega \\ &= \int_{\Omega} \frac{\partial f}{\partial \phi_i} \eta + \kappa (\nabla \phi_i \cdot \nabla \eta) d\Omega \\ &= \int_{\Omega} \left(\frac{\partial f}{\partial \phi_i} - \kappa \Delta \phi_i \right) \eta d\Omega. \end{aligned} \quad (3)$$

Between the third and fourth lines of Eq.(3), the divergence theorem is applied and the homogeneous Neumann boundary condition ($\nabla \phi_i \cdot \mathbf{n} = 0$) is imposed. We therefore obtain the Allen–Cahn type equation [62]

$$\frac{\partial \phi_i}{\partial t} + M_i \left(\frac{\partial f(\{\phi\}, T)}{\partial \phi_i} - \kappa \Delta \phi_i \right) = 0. \quad (4)$$

This provides the solvable form of the equation. Next, we specify the explicit form of the free energy function $f(\{\phi\}, T)$, we adopt the form proposed in [30]

$$\begin{aligned} f(\{\phi\}, T) &= W \left[\sum_{i=0}^N \left(\frac{\phi_i^4}{4} - \frac{\phi_i^2}{2} \right) + \gamma_{PF} \sum_{i=0}^N \sum_{j>i}^N \phi_i^2 \phi_j^2 + \frac{1}{4} \right] \\ &\quad + L \frac{T_{Liq} - T}{T_{Liq}} h(\{\phi\}), \end{aligned} \quad (5)$$

where W is the height of the multiwell energy, γ_{PF} is the penalty coefficient that prevents OPs from overlap, L is the latent, and T_{Liq} is the liquidus temperature. The first term uses a classic form of potential to promote phase separation. The γ_{PF} term is introduced to penalize the overlap between different phases, and latent term allows temperature to drive the phase transformation. The portion of the latent heat term excluding the interpolation function $h(\{\phi\})$ follows the Steinbach type formulation [63]. It effectively shifts the energy minimum upward or downward depending on the deviation of the interface temperature from the melting point. Any deviation from the melting temperature energetically favors either the solid or the liquid phase.

In the latent term of Eq.(5), $h(\{\phi\})$ serves as an interpolation function that defines the local driving force for solidification, which is taken as [30]

$$h(\{\phi\}) = \frac{p_0(\phi_0)}{\sum_{i=0}^N p_i(\phi_i)}, \quad (6)$$

where $p_i(\phi_i)$ is an interpolation function for i th OP, it is a smooth interpolation function used to model the transition between the internal energy densities of the solid and liquid phases [64]. Equation. (6) is a Moelans-type interpolation [65], equal to zero in the solid and one in the liquid. It is normalized and smooth, providing thermodynamic consistency and improved numerical stability. We adopt a thermodynamically stable form for the interpolation function according to [64], which reads

$$p_i(\phi_i) = \phi_i^3(20 - 45\phi_i + 36\phi_i^2 - 10\phi_i^3). \quad (7)$$

After obtaining the form of $p_i(\phi_i)$, we note that the phase field equation inherently drives the total free energy functional E to decrease over time. Consequently, in the latent heat term, when the temperature is above the liquidus temperature T_{Liq} , ϕ_0 tends to increase.

Remark: In their original work [30], they followed the variable transformation proposed in [66], converting the OP into a pseudo signed distance function (PSDF). All parameter settings in their study are based on the PSDF formulation. In contrast, the present work does not apply such a transformation; all equations, parameter settings, and numerical solutions are based on the original OP formulation.

2.3. Model parameters

To perform numerical simulations, the following model parameters are defined based on experimental data and the references [67]. We define $\gamma_{PF} = \frac{3}{2}$, $W = \frac{6\gamma_{SL}}{\zeta}$ and $\kappa = \frac{9\gamma_{SL}\zeta}{2}$, where ζ is the characteristic length, reflecting the thickness of the transition layer. For the values of M_i , they depend on the positions of the points. We divided the computational domain into three main types of regions, bulk liquid, liquid-solid interface, and bulk solid. M_0 refers to [30]

$$M_0 = L_{AC}(\{\phi\}), \quad (8)$$

where $L_{AC}(\{\phi\})$ is determined as the weighted average over each pairwise interface mobility [67]. And $M_{i \neq 0}$ is identified as

$$M_{i \neq 0} = \begin{cases} L_{AC}(\{\phi\}), & \phi_0 \geq -\phi_c \\ L_b^s, & \phi_0 < -\phi_c, \end{cases} \quad (9)$$

where L_b^s is a small bulk mobility, and ϕ_c is the lower bound of the liquid-solid interface. In practice, L_{AC} is applied in the solid-liquid interface region to drive the evolution of the phase-field variable, while L_b^s is used in the bulk solid region. A relatively large value of L_{AC} is chosen to capture the rapid dynamics at the solid-liquid interface. Following the formulation by Moelans et al [67]. $L_{AC}(\{\phi\})$ is expressed as a weighted sum of individual pairwise interface mobilities

$$L_{AC}(\{\phi\}) = \frac{\sum_{i=0}^N \sum_{j>i}^N L_{ij} \phi_i^2 \phi_j^2}{\sum_{i=0}^N \sum_{j>i}^N \phi_i^2 \phi_j^2}, \quad (10)$$

where L_{ij} is the phase field mobility between ϕ_i and ϕ_j . This mobility formulation allows the model to resolve interface kinetics between each pair of phases through L_{ij} while the weight $\phi_i^2 \phi_j^2$ ensures that each mobility term is only active in the region where both phases coexist. This structure accurately reflects the pairwise competition between phases. Furthermore, the normalization ensures consistency and boundedness of the effective mobility. The form of L_{AC}

indicates that it is nonzero only in the interfacial layer and zero within the bulk of each phase. For liquid-solid pairs of OPs, the L_{ij} denotes

$$L_{ij} \frac{3\zeta L}{T_{Liq}} = \begin{cases} 2\mu_{ij}, & \frac{\partial T}{\partial t} \leq 0 \\ 4\mu_0, & \frac{\partial T}{\partial t} > 0 \end{cases} \quad (11)$$

where μ_{ij} denotes the orientation-dependent mobility of the interface between phases i and j , and μ_0 represents the baseline magnitude of mobility. The coefficient L_{ij} directly determines the interface mobility. As indicated by the formulation, a thicker interface and a larger latent heat result in a lower interface migration rate under a given thermal driving force, which aligns with physical intuition. For solid–solid phase pairs, L_{ij} represents

$$L_{ij} = \min(L_{0k}, L_{k0}), \quad (12)$$

for $i \neq 0$ and $j \neq 0$. This equation assumes that the grain boundary (GB) mobility near the solid–liquid interface is comparable in magnitude to the solid–liquid interfacial mobility, allowing triple junctions to rotate. However, the GB mobility rapidly decreases in the bulk region, away from the melt pool interface. Consistent with [30], $L_b^s = \frac{\mu_0 T_{Liq}}{150\zeta L}$ is used to reduce grain coarsening while avoiding numerical artifacts. And μ_{ij} is considered orientation-dependent for solid-liquid interfaces

$$\mu_{ij}(\mathbf{n}_{ij}) = \mu_0 [1 + \epsilon_4 (4(n_{1,ij}^4 + n_{2,ij}^4 + n_{3,ij}^4) - 3)], \quad (13)$$

where ϵ_4 is the anisotropy parameter and $\mathbf{n}_{ij} = n_{1,ij}\hat{\mathbf{e}}_1 + n_{2,ij}\hat{\mathbf{e}}_2 + n_{3,ij}\hat{\mathbf{e}}_3$ denotes the normal vector of the solid-liquid interface in the coordinate frame of the solid domain. For each pair of order parameters, the normal vector is computed as

$$\mathbf{n}_{ij} = \frac{\nabla\phi_i - \nabla\phi_j}{|\nabla\phi_i - \nabla\phi_j|}. \quad (14)$$

Combined, Eqs.(8)–(14) indicate that the mobility for ϕ_0 is nonzero only at the solid–liquid interface. It vanishes within the liquid phase and in regions far from the interface, implying that ϕ_0 needs to be updated only near the solid–liquid interface during computation. Similarly, for ϕ_i updates are required only at the solid–solid grain boundaries, since the values within the solid interior remain unchanged even if the mobility is nonzero.

2.4. Semi-discretized finite element formulation

To solve Eq.(4) using the finite element method, we first derive its weak form. Assuming the homogeneous Neumann boundary condition applies to the problem, we can get the weak form as

$$\int_{\Omega} \delta\phi \frac{\partial\phi_i}{\partial t} d\Omega + \int_{\Omega} \delta\phi M_i \frac{\partial f(\{\phi\}, T)}{\partial\phi_i} d\Omega + \int_{\Omega} \nabla\delta\phi \cdot M_{i\kappa} \nabla\phi_i d\Omega = 0, \quad \forall t \in [0, t_1], \quad (15)$$

where t_1 is the final time, and $\delta\phi$ is the test function. Eq.(14) can be discretized using a finite element approximation

$$\phi_h = \sum_{p \in S} N_p \phi_p = \mathbf{N}\boldsymbol{\phi}, \quad (16)$$

where S represents the set of supporting nodes of the FE shape functions, N_p is the nodal shape function, ϕ_p is the nodal solution, \mathbf{N} and $\boldsymbol{\phi}$ are the vector of the N_p and ϕ_p . Consider Eq.(15) holds for the arbitrary $\delta\phi$, and using this definition, Eq.(14) can be rewritten as follows

$$\int_{\Omega} \mathbf{N}^T \frac{\partial\phi_i}{\partial t} d\Omega + \int_{\Omega} \mathbf{N}^T M_i w(\phi, \phi_i) d\Omega + \int_{\Omega} \mathbf{B}^T M_{i\kappa} \mathbf{B}\boldsymbol{\phi}_i d\Omega = 0, \quad \forall t \in [0, t_1], \quad (17)$$

where $w(\phi, \phi_i) = \frac{\partial f}{\partial\phi_i}$. Equation (17) shows that the main computational cost arises from three components: mobility calculation, energy evaluation, and time integration. As discussed at the end of the previous section, the first two components can be computed only near the interfaces to reduce computational expense.

3. The proposed time integration scheme

3.1. Revisited discrete energy law

Since the phase field equation describes a gradient flow that minimizes the free energy, it is expected to satisfy an energy law. By taking L^2 inner product of Eq.(4) with $(\frac{\partial f}{\partial \phi_i} - \kappa \Delta \phi_i)$, we can find that

$$\int_{\Omega} \frac{\partial \phi_i}{\partial t} \left(\frac{\partial f}{\partial \phi_i} - \kappa \Delta \phi_i \right) d\Omega = - \int_{\Omega} M_i \left(\frac{\partial f}{\partial \phi_i} - \kappa \Delta \phi_i \right)^2 d\Omega. \quad (18)$$

On the other hand, taking the time derivative of E yields

$$\begin{aligned} \frac{dE}{dt} &= \int_{\Omega} \left(\sum_{i=0}^N \frac{\partial f}{\partial \phi_i} \frac{\partial \phi_i}{\partial t} + \frac{\partial f}{\partial T} \frac{\partial T}{\partial t} + \sum_{i=0}^N \kappa \nabla \phi_i \cdot \nabla \frac{\partial \phi_i}{\partial t} \right) d\Omega \\ &= \sum_{i=0}^N \left[\int_{\Omega} \left(\frac{\partial f}{\partial \phi_i} \frac{\partial \phi_i}{\partial t} - \kappa \Delta \phi_i \frac{\partial \phi_i}{\partial t} \right) d\Omega + \int_{\partial \Omega} \frac{\partial \phi_i}{\partial t} \nabla \phi_i \cdot \mathbf{n} d\partial \Omega \right] + \int_{\Omega} \frac{\partial f}{\partial T} \frac{\partial T}{\partial t} d\Omega \\ &= \sum_{i=0}^N \int_{\Omega} \frac{\partial \phi_i}{\partial t} \left(\frac{\partial f}{\partial \phi_i} - \kappa \Delta \phi_i \right) d\Omega + \int_{\Omega} \frac{\partial f}{\partial T} \frac{\partial T}{\partial t} d\Omega \end{aligned} \quad (19)$$

This energy dissipation behavior reflects the thermodynamic consistency of the model, indicating the system's evolution toward lower free energy states. Since the homogeneous free energy $f(\{\phi\}, T)$ is temperature dependent, and our goal is to analyze the influence of $\{\phi\}$ on the energy evolution. We assume the temperature remains constant to eliminate its interference which implies

$$\left. \frac{dE}{dt} \right|_{\frac{\partial T}{\partial t}=0} = \sum_{i=0}^N \int_{\Omega} \frac{\partial \phi_i}{\partial t} \left(\frac{\partial f}{\partial \phi_i} - \kappa \Delta \phi_i \right) d\Omega = - \sum_{i=0}^N \int_{\Omega} M_i \left(\frac{\partial f}{\partial \phi_i} - \kappa \Delta \phi_i \right)^2 d\Omega \leq 0. \quad (20)$$

It is important to note that the derived energy law is strictly valid only when T is constant. Therefore, the total energy can only be meaningfully compared between successive time steps when the temperature remains fixed. Thus, Eq.(20) implies the discrete energy law

$$E(\{\phi^{k+1}\}, T^{k+1}) - E(\{\phi^k\}, T^{k+1}) \leq 0, \quad (21)$$

where k refers the k -th time step. This discrete energy law is expected to be satisfied during the numerical solution process.

3.2. Stabilized semi-implicit time integration

To numerically solve Eq. (16), we adopt a suitable time integration method. Time integration schemes are typically classified into three categories: explicit, implicit, and semi-implicit. Among them, explicit methods such as the forward Euler scheme and explicit Runge–Kutta methods [30], are widely used due to their simplicity and computational efficiency per time step. However, they require extremely small time steps to ensure stability, which significantly increases computational cost in large-scale simulations. Furthermore, explicit methods do not guarantee satisfaction of the energy law, which is critical for long-term physical fidelity.

In contrast, implicit schemes are unconditionally energy-stable and can handle larger time steps. However, they involve solving nonlinear systems at each step, typically requiring multiple inner iterations and often suffering from convergence issues, especially under such a complex energy formulations.

To balance stability and efficiency, we adopt a semi-implicit (or linearly implicit) scheme. This approach avoids nonlinear iteration by solving a linear elliptic equation with constant coefficients at each time step

$$\int_{\Omega} \mathbf{N}^T \frac{\phi_i^{k+1} - \phi_i^k}{\Delta t} d\Omega + \int_{\Omega} \mathbf{N}^T M_i w(\phi^k, \phi_i^k) d\Omega + \int_{\Omega} \mathbf{B}^T M_i \kappa \mathbf{B} \phi_i^{k+1} d\Omega = 0, \quad \forall t \in [0, t_1], \quad (22)$$

where ϕ_i^{k+1} and ϕ_i^k represent the solutions at the current and previous time steps, respectively, and $\Delta t = t^{k+1} - t^k$. This approach avoids nonlinear iteration while maintaining better stability properties than the explicit scheme. However, this scheme also has a step size constraint to satisfy the energy law. It can be written as

$$\Delta t \leq \frac{2}{M_i \max(w')}, \quad (23)$$

where $w' = \frac{\partial w}{\partial \phi_i}$. To overcome this limitation, we adopt a stabilized semi-implicit scheme, which reads

$$\int_{\Omega} \mathbf{N}^T (\phi_i^{k+1} - \phi_i^k) \left(\frac{1}{\Delta t} + \alpha M_i \right) d\Omega + \int_{\Omega} \mathbf{N}^T M_i w(\phi^k, \phi_i^k) d\Omega + \int_{\Omega} \mathbf{B}^T M_{i\kappa} \mathbf{B} \phi_i^{k+1} d\Omega = 0, \quad \forall t \in [0, t_1], \quad (24)$$

where α is a stabilizing coefficient. The derivation for getting α will be presented in the next section. This formulation can be proven to satisfy the energy law for any Δt . To further improve temporal accuracy while preserving energy stability, we employ a second-order stabilized semi-implicit scheme

$$\begin{aligned} \int_{\Omega} \mathbf{N}^T (3\phi_i^{k+1} - 4\phi_i^k + \phi_i^{k-1}) \left(\frac{1}{2\Delta t} \right) d\Omega + \int_{\Omega} \mathbf{N}^T (\phi_i^{k+1} - 2\phi_i^k + \phi_i^{k-1}) (\alpha M_i) d\Omega \\ + \int_{\Omega} \mathbf{N}^T M_i [2w(\phi^k, \phi_i^k) - w(\phi^{k-1}, \phi_i^{k-1})] d\Omega \\ + \int_{\Omega} \mathbf{B}^T M_{i\kappa} \mathbf{B} \phi_i^{k+1} d\Omega = 0, \quad \forall t \in [0, t_1]. \end{aligned} \quad (25)$$

It is important to note that being energetically stable does not imply that the time step Δt can be arbitrarily large without affecting the accuracy of the solution. In practice, a sufficiently small time step is still required to accurately capture the temperature evolution and to maintain the same level of accuracy as in Eq.(21).

3.3. Energy stability analysis

Unlike traditional models, the present formulation involves a highly complex energy functional, and the mobility M_i varies spatially, depending on local physical properties such as phase and temperature. Therefore, it is necessary to carry out an analysis specific to the present model to evaluate its energy stability. To ensure energy stability in the first-order stabilized semi-implicit scheme, the stabilizing parameter α needs to satisfy the following condition

$$\alpha \geq \frac{\max(w')}{2}. \quad (26)$$

In this section ϕ_0 denotes the liquid phase and ϕ_i refers to solid phase. Since the model focuses on grain solidification, we are primarily concerned with ensuring energy stability within the solid phases. Therefore, we will give the second derivative of the homogeneous free energy with respect to the solid phase.

$$\frac{\partial^2 f(\{\phi\}, T)}{\partial \phi_i^2} = w'_i = W[3\phi_i^2 - 1 + \gamma_{PF} \sum_{j \neq i}^N 2\phi_j^2] + L \frac{T_{Liq} - T}{T_{Liq}} \left(-\frac{p_0(\phi_0) * p_i''(\phi_i)}{(\sum_{i=0}^N p_i(\phi_i))^2} + \frac{2p_0(\phi_0) * p_i'^2(\phi_i)}{(\sum_{i=0}^N p_i(\phi_i))^3} \right). \quad (27)$$

We observe that the expression of w' in the present model is highly complex. Although optimization methods such as SLSQP [68] can be employed to determine the extrema of w' , the resulting values are too large and negatively impact the simulation precision. To address this issue, we adopt a simplified form of w' by removing the latent heat term

$$w'_i = W[3\phi_i^2 - 1 + \gamma_{PF} \sum_{j \neq i}^N 2\phi_j^2]^{\gamma_{PF} \equiv 3/2} W[\sum_{j=0}^N 3\phi_j^2 - 1]. \quad (28)$$

Although there is no theoretical constraint enforcing the sum of all phases at a point to equal one, numerical experiments indicate that this sum tends to fluctuate around one in practice. As a result, Eq.(28) implies $w' \leq 2W$, and choosing $\alpha \geq W$ serves as a practical and effective option. We now divide the computational domain into two regions:

Ω_a , where the mobility is L_b^s , corresponding to the bulk solid phase, and Ω_b , which encompasses all areas outside the bulk solid.

In region Ω_a , the value of ϕ_0 is sufficiently small, causing the latent heat term to approach zero. Therefore, it is reasonable to adopt the w'_i as the form given in Eq.(28) for this region. Moreover, since the mobility is a constant, the corresponding energy stability can be rigorously justified if we adopt Eq.(24) as the scheme. The detailed proof is provided in [52]. As for the region Ω_b , the latent term in homogeneous free energy will be relatively larger than other terms, including the gradient energy term, across almost the entire region. This overall dominance is inferred from the design intention of the latent term, explicitly introduced to drive solidification via temperature differences, and is further confirmed by numerical simulations showing that the inclusion of this term effectively governs the directional growth behavior; specifically, under identical mobility conditions, the evolution induced solely by the multiwell term is significantly smaller compared to the evolution driven by the combined multiwell and latent heat terms. Thus, the Eq.(4) will be

$$\frac{\partial \phi_i}{\partial t} = -M_i \left(L \frac{T_{Liq} - T}{T_{Liq}} \frac{\partial h(\{\phi\})}{\partial \phi_i} \right), \quad (29)$$

which implies

$$\frac{\partial \phi_i}{\partial t} = M_i \left(L \frac{T_{Liq} - T}{T_{Liq}} \frac{p_0(\phi_0) * p'_i(\phi_i)}{(\sum_{i=0}^N p_i(\phi_i))^2} \right). \quad (30)$$

In this equation, $T_{Liq} - T$ will directly determine the sign of $\frac{\partial \phi_i}{\partial t}$ (other parts are positive). This means that when the temperature is above the T_{Liq} , the solid phase ϕ_i tends to decrease. Otherwise, ϕ_i increases, promoting solidification. From Eq. (6), it can be seen that $h(\{\phi\})$ is a monotonically decreasing function with respect to the solid phase. When the temperature is below the T_{Liq} , an increase in the ϕ_i leads to a decrease in $h(\{\phi\})$, and consequently, the latent heat term causes a reduction in the total free energy. Conversely, when the temperature is above the T_{Liq} , the ϕ_i decreases, $h(\{\phi\})$ increases, and the total free energy still decreases. Therefore, in regions where the latent heat term dominates the free energy, this term can ensure energy law.

4. Numerical Experiments

As the model accounts for the thermal field, Rosenthal's solution [69] was adopted to describe the temperature evolution in the 3D printing process, the detailed setting is provided in Appendix A. The initial condition for the polycrystalline simulations is generated using Centroidal Voronoi Tessellation (CVT) [70]. In two dimensions, 200 random Voronoi points are used, while in three dimensions, 5000 points are employed. The melt pool region is defined as the set of spatial points where the initial temperature T satisfies $T \geq T_{Liq}$ according to Eq. (B1). To improve the uniformity of the CVT structure, five iterations of Lloyd's algorithm [71] are performed. The commonly used parameters in the numerical experiments are summarized in the table below. In this model, we assume that the γ_{SL} and kinetic parameters (μ_0 and ϵ_4) for 316L stainless steel are assumed to be similar to the austenitic γ -phase of pure iron [30, 72].

Table 1: The physical and kinetic parameters used for simulations

Parameter	Value	Reference
L	$1.9 \times 10^{-9} \text{ J}/\mu\text{m}^3$	[73]
T_{Liq}	1700 K	[73]
γ_{SL}	$2 \times 10^{-13} \text{ J}/\mu\text{m}^2$	[72]
μ_0	$2.17 \times 10^5 \mu\text{m}/\text{s K}$	[72]
ϵ_4	0.11	[72]

4.1. Study of energy stability

This section aims to verify whether the stabilized semi-implicit scheme can ensure the energy stability of region Ω_a under various conditions. A two-dimensional cross section domain consisting solely of region Ω_a , with dimensions

$76.8 \mu\text{m} \times 38.4 \mu\text{m}$, is selected for the simulations. The mesh size is set to 640×320 , with the characteristic length ζ is chosen as $1.7 * \Delta x$. Two different mobility values are selected for testing. The first corresponds to the solid-phase mobility L_b^s under the current parameter settings, while the second adopts a value representative of L_{AC} . For each mobility case, simulations are conducted with two different time step sizes, chosen according to Eq. (23). The primary focus is to compare the performance of the first- and second-order semi-implicit schemes, both with and without the stabilizing term. As shown in Figure 1, an initial grain structure without the presence of a liquid phase was obtained using the CVT algorithm described above.

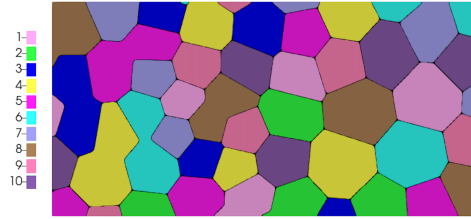
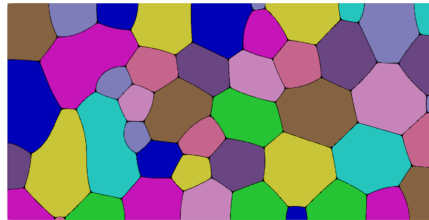
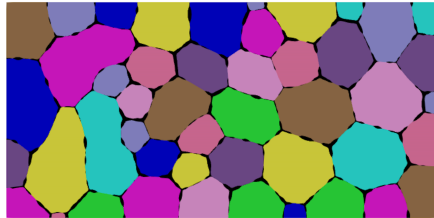


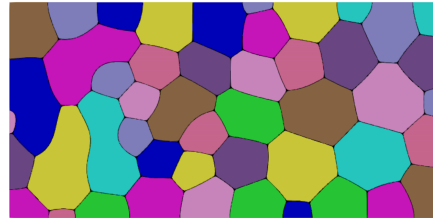
Figure 1: Initial grain structure.



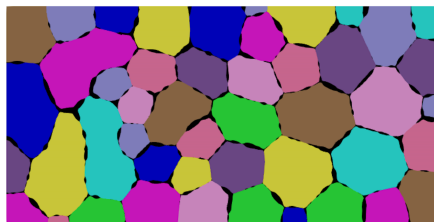
(a) Reference grain structure



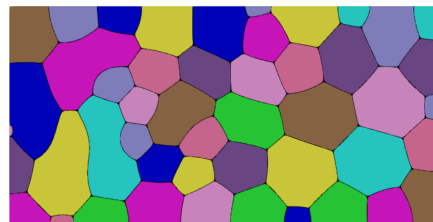
(b) 1st order unstab. semi-impl., $\Delta t = 5 \times 10^{-5}$ s



(c) 1st order stab. semi-impl., $\Delta t = 5 \times 10^{-5}$ s



(d) 2nd order unstab. semi-impl., $\Delta t = 1 \times 10^{-4}$ s



(e) 2nd order stab. semi-impl., $\Delta t = 1 \times 10^{-4}$ s

Figure 2: Grain structure obtained at 0.01 s for the case $L = L_b^s$.

Figure 2(a) shows the reference microstructure after 0.01 s of evolution. This results indicates that the grain structures in the bulk solid region evolves substantially over time. As shown in Figure 2(b)(c), the stabilizing effect of α on energy stability is clearly observed. The results obtained using the stabilized scheme maintain sharp interfaces

and preserve the geometric features consistent with the reference solution. In contrast, the unstabilized scheme yields blurred grain structures.

Due to the naturally larger allowable time step in the second-order semi-implicit scheme, we increased the time step accordingly in the simulations. As shown in Figure 2(d)(e), the stabilizing parameter α also exhibits a significant impact in this higher-order scheme.

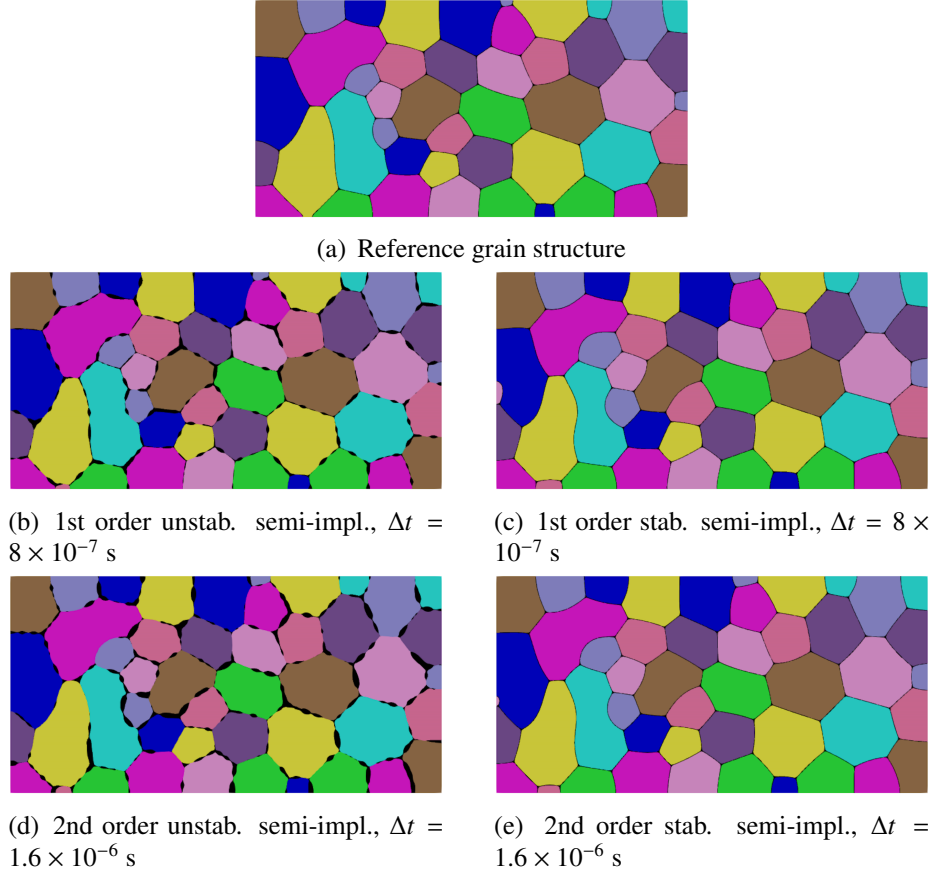


Figure 3: Grain structure obtained at 1.6×10^{-4} s for the case $L = L_{AC}$.

In contrast to the previous group, this set of tests adopts a commonly used mobility value of L_{AC} . Figure 3(a) presents the reference result after an evolution time of 1.6×10^{-4} s. Similar to the results observed in the previous group, Figures 3(b)(c)(d)(e) demonstrate that the stabilizing term effectively guarantees energy stability, thereby relaxing the time step limitation dictated by Eq. (23).

Since no liquid phase is present, the total free energy is independent of temperature, allowing for a direct comparison of energy evolution across time steps. As illustrated in Figure 4, the stabilizing term α ensures a consistent decrease in total free energy.

The pursuit of energy stability under large time steps is motivated by the practical demands of real-scale simulations, where the computational domain is typically divided into two regions: the melt pool region and the area far from the melt pool. The melt pool region corresponds to Ω_a and Ω_b as described in Section 3.3, while the region distant from the melt pool consists entirely of Ω_a , which accounts for the vast majority of the domain. Due to the relatively small temperature variations and the absence of liquid phase in this distant region, larger time steps can be adopted to reduce computational cost. The introduction of the stabilizing term not only enables stable simulations in these regions with large time steps, but also significantly improves the allowable time step size within the melt pool region.

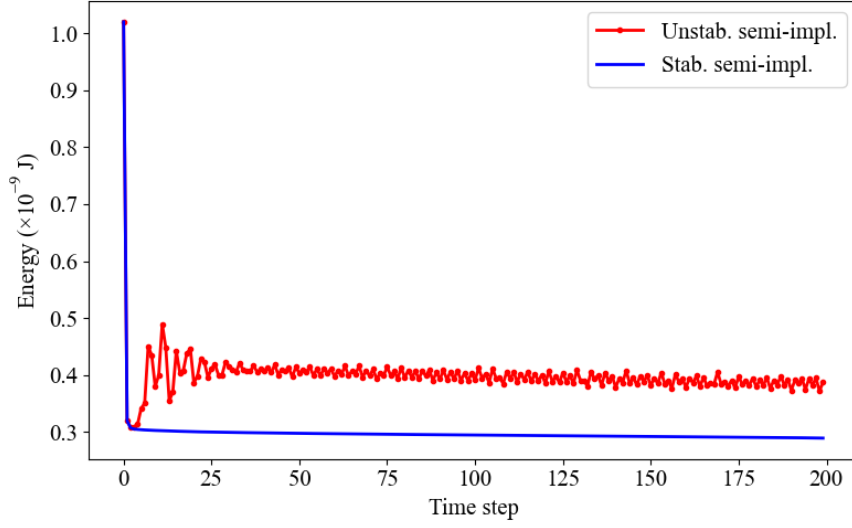


Figure 4: Energy evolution

4.2. Performance comparison under varying time steps

Next, we test the performance of each scheme under varying time step sizes. We adopt a similar problem setup as in the previous section, but this case includes a liquid phase. In addition, the temperature is held while a stabilized semi-implicit scheme is used to evolve the system for $1 \mu\text{s}$, in order to generate the initial diffuse microstructure. The total simulation time is $60 \mu\text{s}$. Figure 5 presents the reference results obtained using the second-order semi-implicit

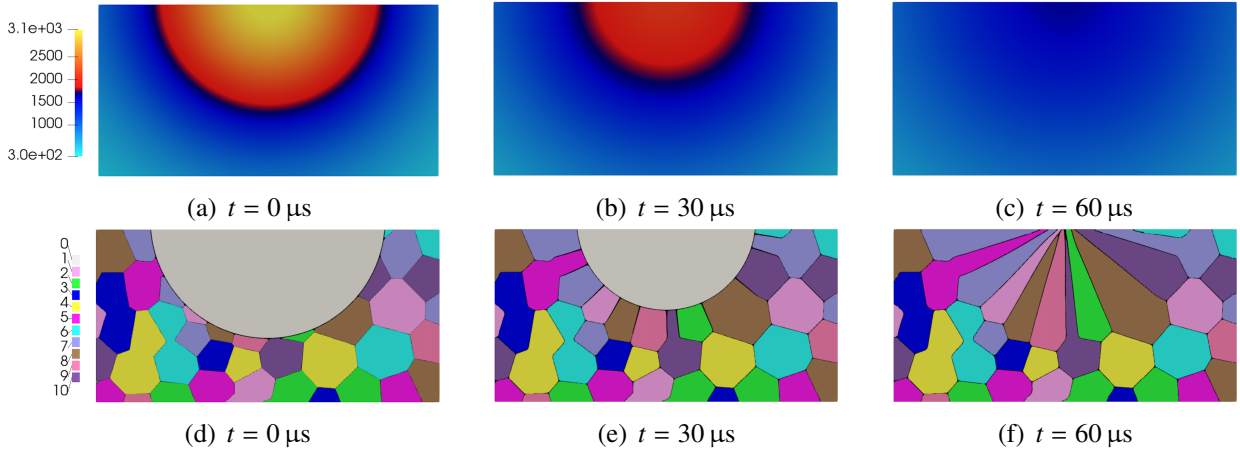


Figure 5: Reference temperature field and grain structure at different time

scheme with a small time step. It illustrates the evolution of grain structures in response to temperature changes. The grains are observed to grow along the direction of the negative temperature gradient.

Figure 6 presents the microstructure evolution results obtained using a first-order explicit method with different time step sizes. At a time step of 5×10^{-9} s, the result closely matches the reference solution. However, as shown in figure 6(b), the simulation exhibits significant inaccuracies. With larger time steps, the results become entirely wrong. We found that the stability threshold for the traditional explicit scheme under the current conditions is on the order of 1–10 nanoseconds, which is consistent with the findings reported in [30].

As shown in Figure 7 and Figure 8, the stabilized semi-implicit schemes permit significantly larger time steps

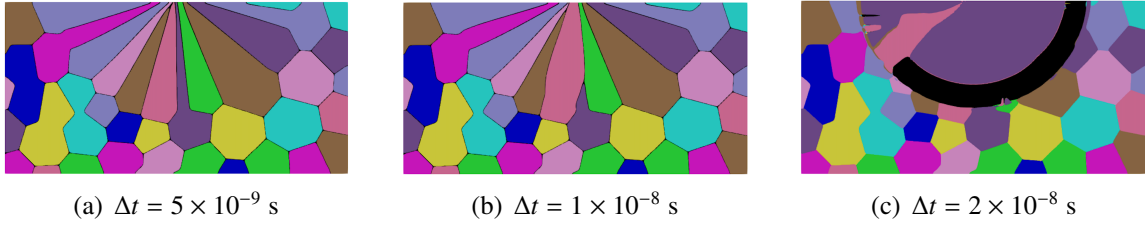


Figure 6: Microstructure results for the expl. method under varying time step sizes

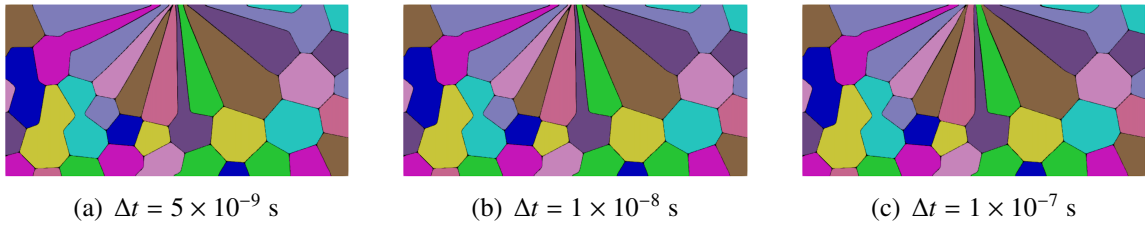


Figure 7: Microstructure results for the 1st order stab. semi-impl. under varying time step sizes

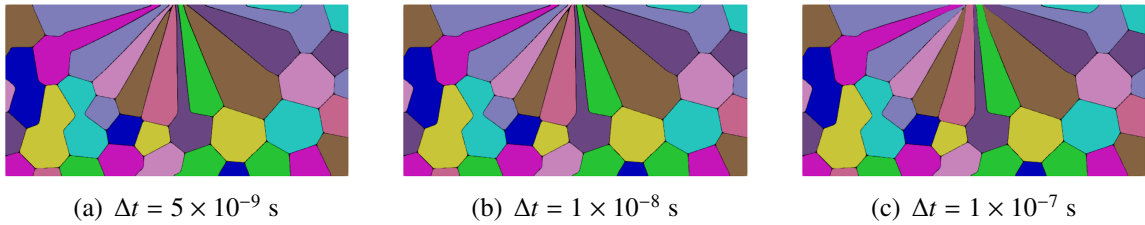


Figure 8: Microstructure results for the 2nd order stab. semi-impl. under varying time step sizes

compared to the traditional explicit method. All tested schemes successfully reach a time step size of 100 nanoseconds while still producing grain structures that closely match the reference solution, demonstrating the superior stability of semi-implicit methods within the current model framework.

This represents an improvement of nearly two orders of magnitude over the explicit method, leading to a substantial reduction in computational cost. Although the semi-implicit schemes require solving a linear system at each time step, this overhead can be mitigated using narrow-band techniques and tensor decomposition methods.

In addition, we tested the results of both first- and second-order unstabilized semi-implicit schemes. The results show that both schemes perform well at a time step of 1×10^{-7} s, but begin to exhibit instabilities at larger time steps. To further investigate this behavior, we also examined results at 3×10^{-7} s. It is worth noting that these results were obtained using a mixed time-stepping approach. Specifically, during phases of intense phase competition, a smaller time step such as 1×10^{-7} s was used to effectively capture the evolving dynamics. The corresponding results are presented in Figure 9.

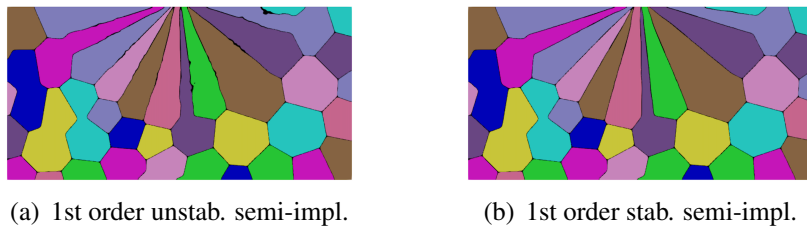


Figure 9: Stabilization effect of α at large time step size ($\Delta t = 3 \times 10^{-7}$ s).

Figure 9 demonstrates that the inclusion of the stabilization term α significantly enhances numerical stability under large time step conditions. These results further confirm the superior performance of the stabilized semi-implicit scheme within the current model framework. To quantitatively assess the accuracy of different time integration schemes, we next evaluate the relative L^2 norm of the error at each time step with respect to a reference solution. The error is defined as

$$e_0 = \frac{(\sum_{i=1}^N \|\phi_{r,i} - \phi_{h,i}\|_{L^2(\Omega)}^2)^{0.5}}{(\sum_{i=1}^N \|\phi_{r,i}\|_{L^2(\Omega)}^2)^{0.5}} \quad (31)$$

where $\phi_{r,i}$ denotes the reference solution, and $\phi_{h,i}$ refers the numerical solution obtained from the scheme being evaluated. The solution obtained using the second-order semi-implicit scheme with a small time step is used as the reference solution in these comparisons.

Figure 10 shows that all three time integration schemes yield good accuracy at small time steps. However, the second-order stabilized semi-implicit scheme exhibits the highest accuracy, followed by the first-order stabilized semi-implicit scheme, with the explicit method performing the worst. When the time step reaches the order of 10 nanoseconds, the error of the explicit scheme increases dramatically, whereas the other two methods continue to produce reliable results. This observation is consistent with previous conclusions, highlighting that the stabilized semi-implicit schemes significantly enhance the allowable time step in the current model.

Figure 11 illustrates the free energy change at each time step prior to the completion of solidification in the cross-section, using first- and second-order stabilized semi-implicit schemes with a time step of 100 ns. As all values are negative, the energy law (Eq. (21)) is consistently satisfied. Moreover, the second-order scheme exhibits smoother and more stable energy decay compared to the first-order scheme.

4.3. 3D phase field simulations

We now proceed to evaluate the performance of the proposed model in three-dimensional simulations. A rectangular domain with dimensions $96 \mu\text{m} \times 76.8 \mu\text{m} \times 38.4 \mu\text{m}$ is selected as the computational domain. The mesh is discretized with a resolution of $400 \times 320 \times 160$, and the characteristic length ζ is chosen to be consistent with that used in Section 4.1. We need to mention that we don't need to hold the temperature profile for getting the initial diffuse microstructure. This simulation replicates the behavior of a single laser scan conducted on a polycrystalline baseplate without the presence of a powder layer.

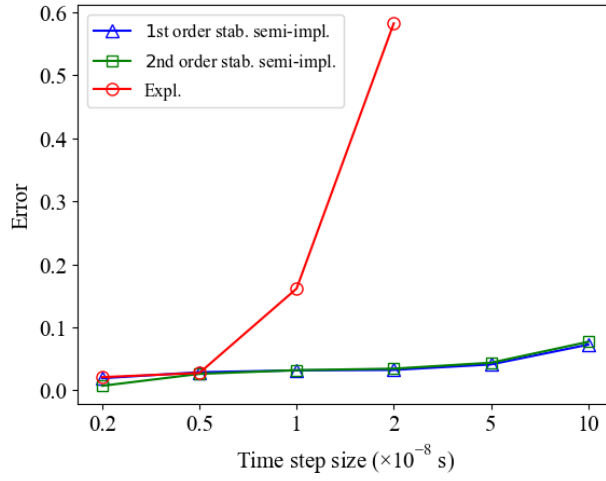


Figure 10: Error analysis

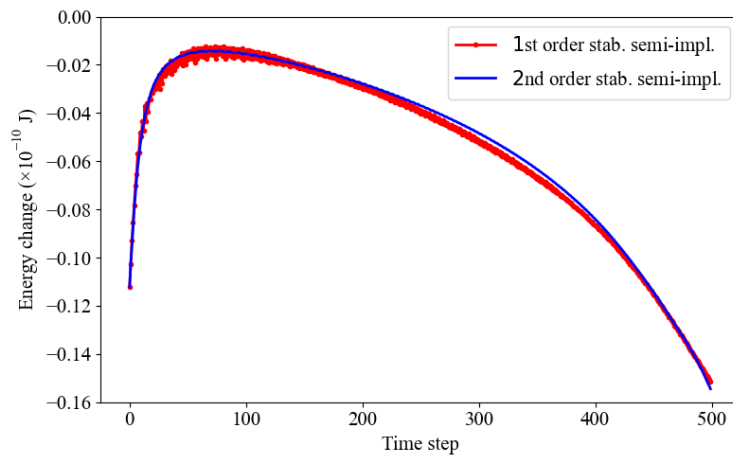


Figure 11: Energy evolution

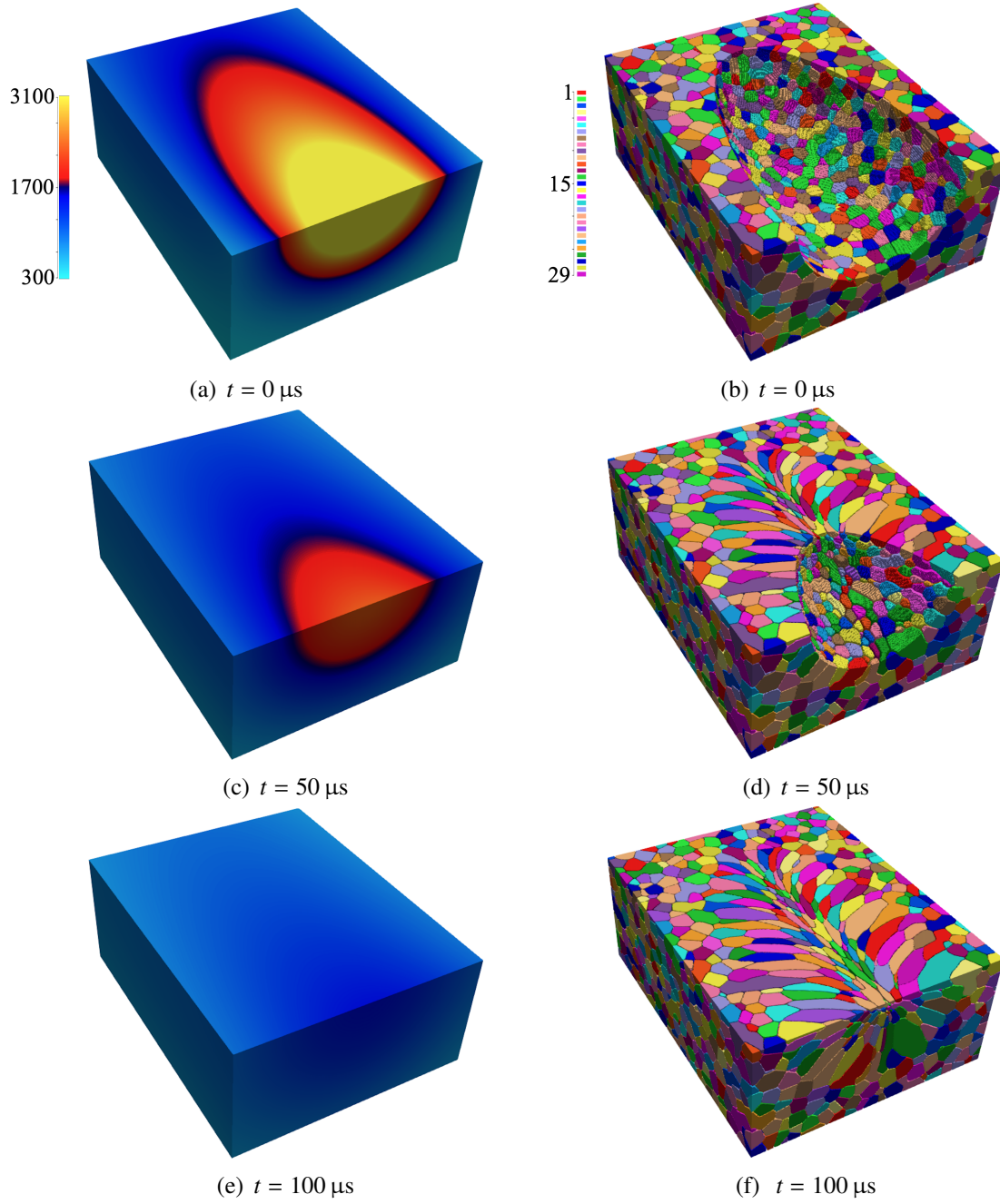


Figure 12: 3D grain structure and temperature field at different time, (a), (c), and (e) show the temperature fields, while (b), (d), and (f) depict the corresponding grain structures.

Figure 12 illustrates the microstructural evolution at (b) 0 μs , (d) 50 μs , and (f) 100 μs . Each grain structure is associated with a corresponding temperature profile. These results are obtained using A first-order stabilized semi-implicit scheme with a time step of 1×10^{-7} s. As the laser progresses, grains begin to solidify along the trailing edge of the melt pool. Eventually, an elongated grain morphology forms, characterized by grains curving from the sides of the melt pool toward the center of the laser track.

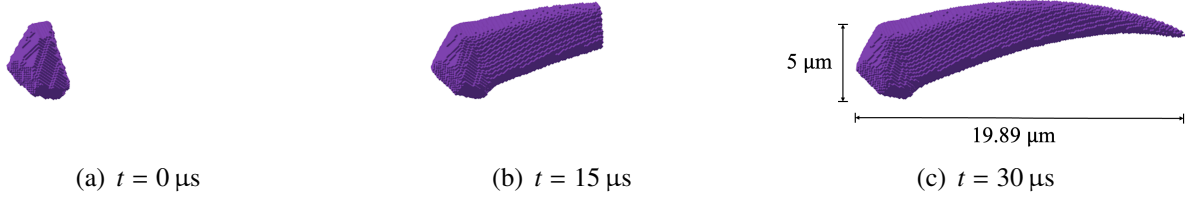


Figure 13: Individual grain

Figure 13 shows the temporal evolution of a typical selected grain extracted from the three-dimensional simulation domain. At $t = 0 \mu\text{s}$, the selected grain exhibits a compact, roughly equiaxed morphology. As time progresses, the grain grows preferentially along the thermal gradient direction, developing a pronounced elongated shape. By $t = 30 \mu\text{s}$, the grain exhibits a larger aspect ratio compared to its initial shape, along with strong directional growth and pronounced curvature. This behavior is highly consistent with the solidification characteristics described in [30].

Furthermore, to validate the effectiveness of the proposed algorithm, we conducted additional comparative studies with different parameters like anisotropy parameter and laser scanning speed. We first present two representative subsets of the top surface microstructures, which differ only in the setting of the kinetic anisotropy parameter. To enhance the visual contrast, this set of simulations uses larger initial grain sizes, generated from 2,500 random Voronoi seed points. In Figure 14, the light green, dark yellow, and dark blue grains slightly left of center are particularly representative. When $\epsilon_4 = 0$ (i.e., isotropic), their grain boundaries appear smooth and extend closer toward the melt pool centerline. As ϵ_4 increases, however, the grain boundaries become straighter and more angular. Grain growth becomes increasingly constrained and is often truncated by neighboring grains with more favorable growth orientations.

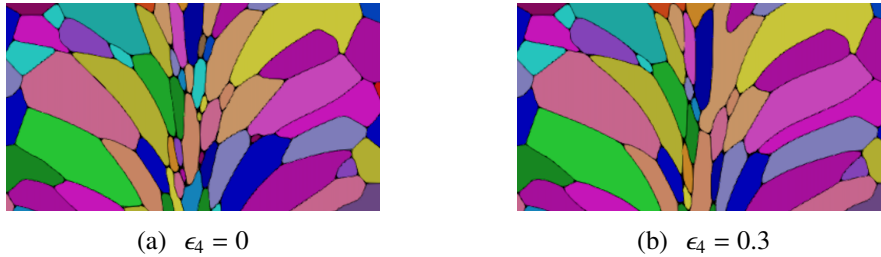
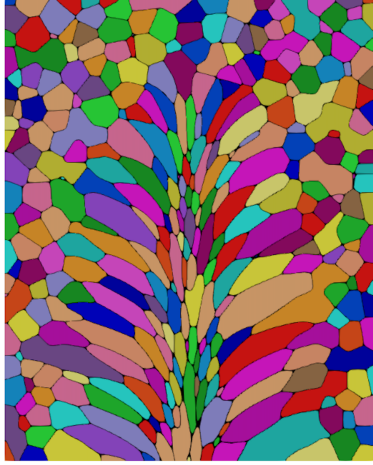


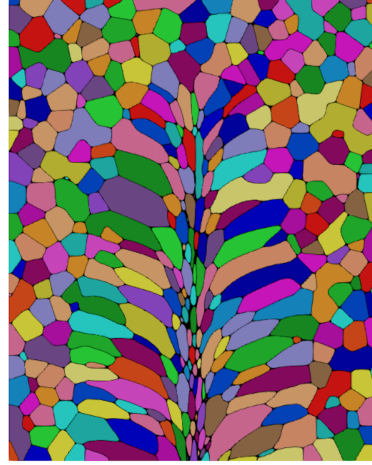
Figure 14: Selected top surface grain structures for (a) $\epsilon_4=0$, (b) $\epsilon_4=0.3$.

This phenomenon arises because increasing ϵ_4 in Eq. (13) amplifies the variation in growth rates along different orientations. As a result, grain boundaries become straighter, grains exhibit more angular morphologies, and those with less favorable orientations are more likely to be overtaken by neighboring grains. This leads to increased grain faceting and intensified in-plane competitive growth. This observation is in agreement with the conclusions drawn in [30]. Then, we demonstrate two visualized cases with different laser scanning speeds. These cases were identical in all other aspects, allowing for a focused examination of the influence of scan speed. We extracted both the top surfaces and longitudinal cross-sections along the scanning direction for analysis.

At constant laser power, increasing the scan speed reduces the melt pool's depth and width. As shown in Figure 15, changes in scan speed significantly affect the final grain structure. Combined with Figure 16, it can be observed that higher scan speeds lead to a reduction in grain curvature and enhance the competitive advantage of grains oriented along the scan direction. This is due to the smaller melt pool and faster solidification, which shorten the growth

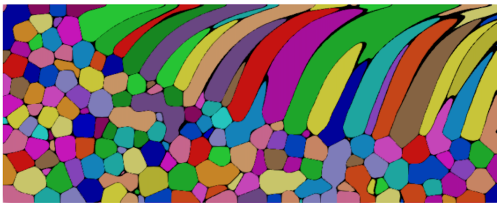


(a) $V_p = 1.0$ m/s

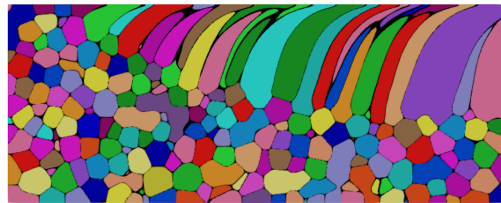


(b) $V_p = 1.5$ m/s

Figure 15: Grain structure of the top surface under different scan velocity.



(a) $V_p = 1.0$ m/s



(b) $V_p = 1.5$ m/s

Figure 16: Grain structure of selected cross sections under different scan velocity.

time and limit lateral grain competition. As a result, only grains aligned with the scan direction can effectively advance the solidification front, while the curved growth seen at lower speeds becomes suppressed. Furthermore, it appears that only a small portion of grains interacting with the melt pool boundaries undergo appreciable growth or shrinkage. These trends are consistent with the experimental and simulation results reported in [31]. These results also demonstrate that certain process parameters in additive manufacturing can significantly influence the final grain structure.

Furthermore, we analyzed a set of 3D simulations with varying scan speeds using the same geometric feature-based statistical framework proposed in [31, 74]. To extract individual grains, we first construct a directed graph of the grain network in sparse matrix form, then apply the 'connected components' from the Scipy package to identify the strongly connected components and thereby segment the individual grains [75]. For each grain, we define an indicator function $D(r)$ such that

$$D(r) = \begin{cases} 1, & r \text{ inside the object} \\ 0, & r \text{ outside the object.} \end{cases} \quad (32)$$

Using this definition, we compute the 3D central moments with respect to the grain's centroid (x_n, y_n, z_n) as

$$v_{ijk} = \int_V (x - x_n)^i (y - y_n)^j (z - z_n)^k D(r) dV. \quad (33)$$

The second-order central moments form a symmetric tensor

$$\mathcal{I} = \begin{pmatrix} v_{020} + v_{002} & -v_{110} & -v_{101} \\ -v_{110} & v_{200} + v_{002} & -v_{011} \\ -v_{101} & -v_{011} & v_{200} + v_{020} \end{pmatrix}, \quad (34)$$

which resembles an inertia tensor and characterizes the spatial distribution of the grain mass. We then perform eigen-decomposition of the central moment tensor \mathcal{I} , yielding $\mathcal{I} = \mathbf{\Upsilon} \mathbf{A} \mathbf{\Upsilon}^{-1}$, where $\mathbf{\Upsilon}$ is an orthogonal matrix whose columns represent the principal axes, and \mathbf{A} is a diagonal matrix representing the moment tensor in the principal axes coordinate system, which reads

$$\mathbf{A} = \begin{pmatrix} \bar{v}_{020} + \bar{v}_{002} & 0 & 0 \\ 0 & \bar{v}_{200} + \bar{v}_{002} & 0 \\ 0 & 0 & \bar{v}_{200} + \bar{v}_{020} \end{pmatrix}, \quad (35)$$

where \bar{v}_{ijk} is the central moments in the principal axes coordinates. We then calculate the \bar{v}_{ijk} using eigenvalues

$$\begin{aligned} \bar{v}_{200} &= \frac{1}{2}(\lambda_2 + \lambda_3 - \lambda_1) \\ \bar{v}_{020} &= \frac{1}{2}(\lambda_1 + \lambda_3 - \lambda_2) \\ \bar{v}_{002} &= \frac{1}{2}(\lambda_1 + \lambda_2 - \lambda_3), \end{aligned} \quad (36)$$

where λ_i is the eigenvalue of matrix \mathcal{I} . Based on the computed central moments, the semi-axes lengths of the equivalent ellipsoid are given by $a = (5\bar{v}_{200}/V)^{0.5}$, $b = (5\bar{v}_{020}/V)^{0.5}$ and $c = (5\bar{v}_{002}/V)^{0.5}$, where V is the volume of the grain. These values are then doubled to obtain the full lengths of the major, median, and minor axes of the grain.

Figure 17 presents the empirical cumulative distribution functions (ECDF) of the major, intermediate, and minor axes across all grains, for a selected set of representative laser scanning speeds (0.75 m/s, 1.00 m/s, 1.50 m/s, 2.00 m/s) [76]. From the figure, it is evident that only the major axis shows significant variation with changing laser scanning speed. Among the selected conditions, the scan speed of 0.75 m/s results in the longest average grain size, while 2.00 m/s produces the shortest. This trend aligns with the physical expectation that a larger melt pool allows for slower cooling and thus promotes greater grain growth. In contrast, the intermediate and minor axes exhibit no noticeable separation across scan speeds. We can find that the scanning speed primarily influences the grain's major axis by modifying the melt pool dimensions, while its effect on the other two axes is minimal. These observations are consistent with findings reported in the literature [31].

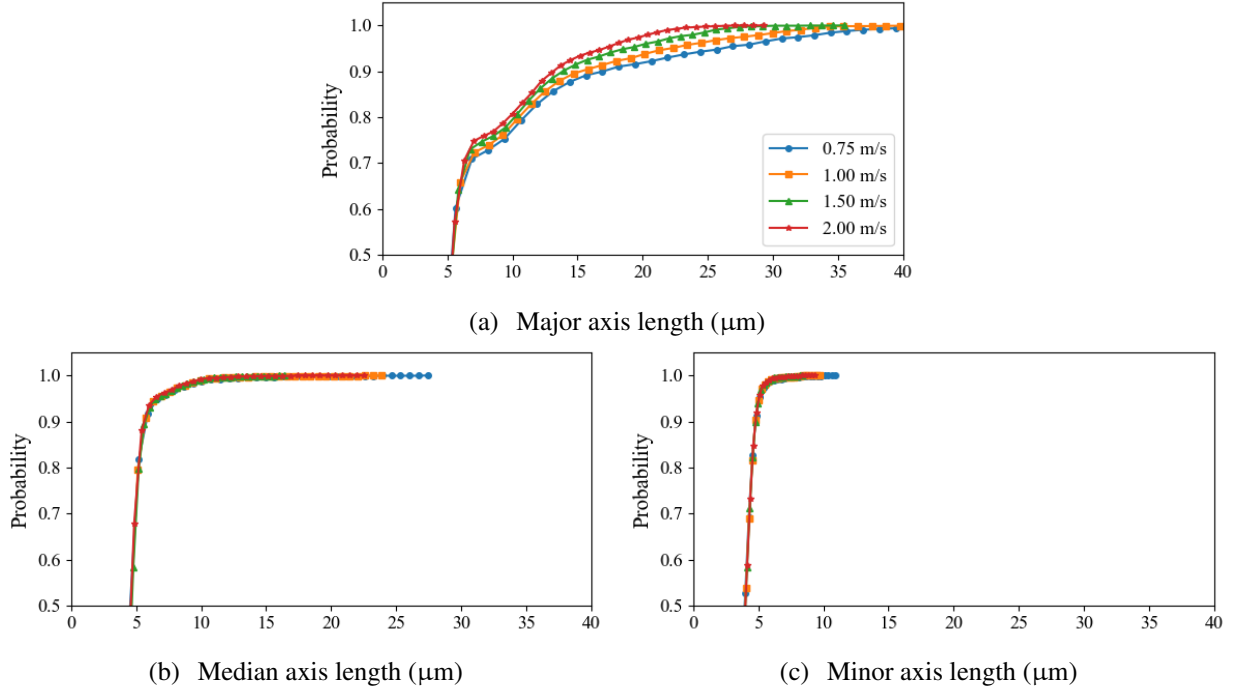


Figure 17: Empirical cumulative distribution functions of the (a) major, (b) median, and (c) minor axes lengths for the simulated tracks.

As the primary focus of this work is to develop an efficient and energy-stable time integration scheme, detailed investigations into process-structure relationships are beyond the scope of this paper. The presented numerical experiments are designed to validate the accuracy and efficiency of the proposed method. In the three-dimensional case, our stabilized semi-implicit scheme achieves a speedup of approximately two orders of magnitude compared to conventional explicit methods. This improvement is particularly valuable for simulating microstructural evolution and optimizing process parameters in additive manufacturing.

5. Conclusion

This work proposed a class of stabilized semi-implicit time integration schemes for phase field simulations of grain growth during rapid solidification in AM processes. The key findings are summarized as follows.

1. The developed stabilized semi-implicit schemes can enable two orders-of-magnitude larger time steps than the conventional explicit scheme without sacrificing the accuracy, a speed-up of the same can be expected.
2. The proposed choice of the stabilization coefficient, along with the stability analysis, can ensure the revisited energy law, as confirmed by the numerical experiments.
3. The proposed method can accurately capture detailed microstructure evolution, including the grain morphology and growth characteristics observed in rapid solidification during AM processes.
4. Both the first-order and second-order stabilized semi-implicit schemes showed superior performance in terms of accuracy and stability.
5. The simulations and numerical results are validated by investigating the effects of kinetic anisotropy and different laser scan speeds and are consistent with that reported in the literature [30].

Our ongoing work is to incorporate convolution tensor decomposition [52] to further accelerate large volume phase field simulations. Additionally, adaptive time-stepping strategies can be developed with the proposed methods. These advancements will enable efficient high fidelity microstructure simulations and ultimately support the improvement of 3D printing processes.

CRediT authorship contribution statement

Acknowledgements

CY and YL would like to acknowledge the support of University of Maryland Baltimore County through the startup fund and the COEIT Interdisciplinary Project Award.

Appendix A. Thermal field

For the temperature profile, we follow the settings in [30], which reads

$$T(X, R) = T_0 + \frac{Q}{2\pi\kappa_T} \left(\frac{1}{R} \right) \exp \left[-\frac{V_P}{2c} (R + X) \right], \quad (\text{A.1})$$

where T_0 denotes the environment temperature, Q is the absorbed heat power from the source, κ_T is the thermal conductivity, c is the thermal diffusivity, and V_P is the velocity of the moving heat source.

In this equation, $R = \sqrt{X^2 + Y^2 + Z^2}$ represents the radial distance from the heat source, where X , Y , and Z are the spatial coordinates in the moving reference frame. And it can be related to the simulation frame with $X = x - x_0 - V_P * t$, $Y = y$ and $Z = z - z_0$, where x , y , and z are the simulation coordinates and x_0 , z_0 are initial coordinates of the heat source. The parameters of Rosenthal's solution are given in following table. Scipioni Bertoli et al. showed that, for PBF of 316L stainless steel, the Rosenthal model provides cooling rate predictions that align closely with experimental measurements and more advanced thermal modeling approaches [77].

Table A.2: The default parameters for Rosenthal's solution

Parameter	Value	Reference
κ_T	$2.7 \times 10^{-5} \text{ W } \mu\text{m K}$	[73]
c	$5.2 \times 10^6 \text{ } \mu\text{m}^2/\text{s}$	[73]
Q	25 W	
V_P	$10^6 \text{ } \mu\text{m}/\text{s}$	
T_0	300 K	
x_0	50 (120) μm	
z_0	21.2 μm	

In this table, the value of x_0 is set to 50 μm in the 2D model, while it is 120 μm in the 3D model.

References

- [1] W. E. Frazier, Metal additive manufacturing: A review, *Journal of Materials Engineering and Performance* 23 (2014) 1917–1928. doi:10.1007/s11665-014-0958-z.
- [2] I. Gibson, D. W. Rosen, B. Stucker, *Additive Manufacturing Technologies: 3D Printing, Rapid Prototyping, and Direct Digital Manufacturing*, 2nd ed., Springer, New York, 2015. doi:10.1007/978-1-4939-2113-3.
- [3] D. Herzog, V. Seyda, E. Wycisk, C. Emmelmann, Additive manufacturing of metals, *Acta Materialia* 117 (2016) 371–392. doi:10.1016/j.actamat.2016.07.019.
- [4] Y. M. Wang, T. Voisin, J. T. McKeown, J. Ye, N. P. Calta, Z. Li, Z. Zeng, Y. Zhang, W. Chen, T. T. Roehling, R. T. Ott, M. K. Santala, P. J. Depond, M. J. Matthews, A. V. Hamza, T. Zhu, Additively manufactured hierarchical stainless steels with high strength and ductility, *Nature Materials* 17 (2018) 63–71. doi:10.1038/nmat5021, epub 2017 Oct 30.
- [5] P. Bajaj, A. Hariharan, A. Kini, P. Kürnsteiner, D. Raabe, E. A. Jägle, Steels in additive manufacturing: A review of their microstructure and properties, *Materials Science and Engineering: A* 772 (2020) 138633. doi:10.1016/j.msea.2019.138633.
- [6] M. Armstrong, H. Mehrabi, N. Naveed, An overview of modern metal additive manufacturing technology, *Manufacturing Letters* 32 (2022) 32–36. doi:10.1016/j.mfglet.2022.02.003.
- [7] T. DebRoy, H. L. Wei, J. S. Zuback, T. Mukherjee, J. W. Elmer, J. O. Milewski, A. M. Beese, A. Wilson-Heid, A. De, W. Zhang, Additive manufacturing of metallic components - process, structure and properties, *Progress in Materials Science* 92 (2018) 112–224. doi:10.1016/j.pmatsci.2017.10.001.

- [8] B. Song, X. Zhao, S. Li, C. Han, Q. Wei, S. Wen, J. Liu, Y. Shi, Differences in microstructure and properties between selective laser melting and traditional manufacturing for fabrication of metal parts: a review, *Frontiers of Mechanical Engineering* 10 (2015) 111–125. doi:10.1007/s11465-015-0341-2.
- [9] Z. Wang, T. A. Palmer, A. M. Beese, Effect of processing parameters on microstructure and tensile properties of austenitic stainless steel 3041 made by directed energy deposition additive manufacturing, *Acta Materialia* 110 (2016) 226–235. doi:10.1016/j.actamat.2016.03.019.
- [10] Y. Kok, X. Tan, P. Wang, M. Nai, N. Loh, E. Liu, S. Tor, Anisotropy and heterogeneity of microstructure and mechanical properties in metal additive manufacturing: a critical review, *Materials & Design* 139 (2018) 565–586. doi:10.1016/j.matdes.2017.11.021.
- [11] T. Kurose, Y. Abe, M. Santos, Y. Kanaya, A. Ishigami, S. Tanaka, H. Ito, Influence of the layer directions on the properties of 316L stainless steel parts fabricated through fused deposition of metals, *Materials* 13 (2020) 2493. doi:10.3390/ma13112493.
- [12] C. Guo, S. Li, S. Shi, X. Li, X. Hu, Q. Zhu, R. Ward, Effect of processing parameters on surface roughness, porosity and cracking of as-built In738lc parts fabricated by laser powder bed fusion, *Journal of Materials Processing Technology* 285 (2020) 116788. doi:10.1016/j.jmatprotec.2020.116788.
- [13] M. Li, Y. Bai, X. Gao, L. Cui, Q. Zhou, J. Zhang, M. Zhang, Microstructure and mechanical properties of 308L stainless steel fabricated by laminar plasma additive manufacturing, *Materials Science and Engineering: A* 770 (2020) 138523. doi:10.1016/j.msea.2019.138523.
- [14] T. Henry, M. Morales, D. Cole, C. Shumeyko, J. Riddick, Mechanical behavior of 17–4 ph stainless steel processed by atomic diffusion additive manufacturing, *The International Journal of Advanced Manufacturing Technology* (2021). doi:10.1007/s00170-021-06785-1.
- [15] W. Kurz, M. Rappaz, R. Trivedi, Progress in modelling solidification microstructures in metals and alloys. part ii: Dendrites from 2001 to 2018, *International Materials Reviews* (2020) 1–47. doi:10.1080/09506608.2020.1757894.
- [16] C.-A. GANDIN, J.-L. DESBIOLLES, M. RAPPAZ, P. THEVOZ, A three-dimensional cellular automaton-finite element model for the prediction of solidification grain structures, *Metallurgical and Materials Transactions A* 30 (1999) 3153–3165. doi:10.1007/s11661-999-0226-2.
- [17] O. Zinovieva, A. Zinoviev, V. Ploshikhin, Three-dimensional modeling of the microstructure evolution during metal additive manufacturing, *Computational Materials Science* 141 (2018) 207–220. doi:10.1016/j.commatsci.2017.09.018.
- [18] Y. Lian, Z. Gan, C. Yu, D. Kats, W. Liu, G. Wagner, A cellular automaton finite volume method for microstructure evolution during additive manufacturing, *Materials & Design* 169 (2019) 107672. doi:10.1016/j.matdes.2019.107672.
- [19] Y. Yu, Y. Li, F. Lin, W. Yan, A multi-grid cellular automaton model for simulating dendrite growth and its application in additive manufacturing, *Additive Manufacturing* 47 (2023) 102284. doi:10.1016/j.addma.2021.102284.
- [20] Q. Xie, X. Yan, S. Yin, X. Li, M. Liu, Y. Wang, L. Zhuang, An extended version of cellular automata model for powder bed fusion to unravel the dependence of microstructure on printing areas for Inconel 625, *Additive Manufacturing* 73 (2023) 103676. doi:10.1016/j.addma.2023.103676.
- [21] C. C. Battaile, The kinetic monte carlo method: Foundation, implementation, and application, *Computer Methods in Applied Mechanics and Engineering* 197 (2008) 3386–3398. doi:10.1016/j.cma.2008.03.010.
- [22] T. M. Rodgers, J. D. Madison, V. Tikare, Simulation of metal additive manufacturing microstructures using kinetic monte carlo, *Computational Materials Science* 135 (2017) 78–89. doi:10.1016/j.commatsci.2017.03.053.
- [23] T. M. Rodgers, J. E. Bishop, J. D. Madison, Direct numerical simulation of mechanical response in synthetic additively manufactured microstructures, *Modelling and Simulation in Materials Science and Engineering* 26 (2018). doi:10.1088/1361-651X/aac616.
- [24] K. L. Johnson, T. M. Rodgers, O. D. Underwood, J. D. Madison, K. R. Ford, S. R. Whetten, D. J. Dagle, J. E. Bishop, Simulation and experimental comparison of the thermo-mechanical history and 3d microstructure evolution of 304L stainless steel tubes manufactured using lens, *Computational Mechanics* 61 (2018) 559–574. doi:10.1007/s00466-017-1516-y.
- [25] T. R. Rodgers, D. M. Moser, F. Abdeljawad, O. D. U. Jackson, J. D. Carroll, B. H. Jared, D. S. Bolintineanu, J. A. Mitchell, J. D. Madison, Simulation of powder bed metal additive manufacturing microstructures with coupled finite difference–monte carlo method, *Additive Manufacturing* 41 (2021) 101953. doi:10.1016/j.addma.2021.101953.
- [26] W. Boettinger, J. Warren, C. Beckermann, A. Karma, Phase-field simulation of solidification, *Annual Review of Materials Research* 32 (2002) 163–194.
- [27] T. Keller, G. Lindwall, S. Ghosh, L. Ma, B. Lane, F. Zhang, U. Kattner, E. Lass, J. Heigel, Y. Idell, M. Williams, A. Allen, J. Guyer, L. Levine, Application of finite element, phase-field, and calphad-based methods to additive manufacturing of ni-based superalloys, *Acta Materialia* 139 (2017) 244–253. doi:10.1016/j.actamat.2017.05.003.
- [28] A. V. Dubrov, F. K. Mirzade, V. D. Dubrov, On modeling of heat transfer and molten pool behavior in multi-layer and multi-track laser additive manufacturing process, in: B. Bodermann, K. Frenner, R. M. Silver (Eds.), *Modeling Aspects in Optical Metrology VII*, SPIE, Munich, Germany, 2019, p. 59. doi:10.1117/12.2527605.
- [29] M. Yang, L. Wang, W. Yan, Phase-field modeling of grain evolutions in additive manufacturing from nucleation, growth, to coarsening, *npj Computational Materials* 7 (2021) 56. doi:10.1038/s41524-021-00524-6.
- [30] A. F. Chadwick, P. W. Voorhees, The development of grain structure during additive manufacturing, *Acta Materialia* 211 (2021) 116862.
- [31] A. F. Chadwick, J. G. S. Macías, A. Samaei, G. J. Wagner, M. V. Upadhyay, P. W. Voorhees, On microstructure development during laser melting and resolidification: An experimentally validated simulation study, *Acta Materialia* 282 (2025) 120482. doi:10.1016/j.actamat.2023.120482.
- [32] M. Rappaz, C.-A. Gandin, Probabilistic modelling of microstructure formation in solidification processes, *Acta Metallurgica et Materialia* 41 (1993) 345–360. doi:10.1016/0956-7151(93)90065-Z.
- [33] C.-A. Gandin, M. Rappaz, A coupled finite element-cellular automaton model for the prediction of dendritic grain structures in solidification processes, *Acta Metallurgica et Materialia* 42 (1994) 2233–2246. doi:10.1016/0956-7151(94)90302-6.
- [34] G. J. Merchant, S. H. Davis, Morphological instability in rapid directional solidification, *Acta Metallurgica et Materialia* 38 (1990) 2683–2693.
- [35] L. X. Lu, N. Sridhar, Y. W. Zhang, Phase field simulation of powder bed-based additive manufacturing, *Acta Materialia* 144 (2018) 801–809. doi:10.1016/j.actamat.2017.11.033.
- [36] P. W. Liu, et al., Investigation on evolution mechanisms of site-specific grain structures during metal additive manufacturing, *Journal of*

- Materials Processing Technology 257 (2018) 191–202. doi:10.1016/j.jmatprotec.2018.02.042.
- [37] P. Liu, Z. Wang, Y. Xiao, ..., Insight into the mechanisms of columnar to equiaxed grain transition during metallic additive manufacturing, *Additive Manufacturing* 26 (2019) 22–29. doi:10.1016/j.addma.2018.12.019.
- [38] N. Provatas, N. Goldenfeld, J. Dantzig, Efficient computation of dendritic microstructures using adaptive mesh refinement, *Physical Review Letters* 80 (1998) 3308.
- [39] C.-s. Zhu, S. Xu, L. Feng, D. Han, K.-m. Wang, Phase-field model simulations of alloy directional solidification and seaweed-like microstructure evolution based on adaptive finite element method, *Computational Materials Science* 160 (2019) 53–61.
- [40] S. DeWitt, S. Rudraraju, D. Montiel, W. B. Andrews, K. Thornton, Prisms-pf: A general framework for phase-field modeling with a matrix-free finite element method, *npj Computational Materials* 6 (2020) 29.
- [41] W. Feng, P. Yu, S. Hu, Z.-K. Liu, Q. Du, L.-Q. Chen, Spectral implementation of an adaptive moving mesh method for phase-field equations, *Journal of Computational Physics* 220 (2006) 498–510.
- [42] R. Li, Y. Gao, Z. Chen, Adaptive discontinuous galerkin finite element methods for the allen-cahn equation on polygonal meshes, *Numerical Algorithms* 95 (2024) 1981–2014.
- [43] D. Liu, Y. Wang, Multi-fidelity physics-constrained neural network and its application in materials modeling, *Journal of Mechanical Design* 141 (2019) 121403.
- [44] D. Montes de Oca Zapiain, J. A. Stewart, R. Dingreville, Accelerating phase-field-based microstructure evolution predictions via surrogate models trained by machine learning methods, *npj Computational Materials* 7 (2021) 3.
- [45] I. Peivaste, N. H. Siboni, G. Alahyarizadeh, R. Ghaderi, B. Svendsen, D. Raabe, J. R. Mianroodi, Machine-learning-based surrogate modeling of microstructure evolution using phase-field, *Computational Materials Science* 214 (2022) 111750.
- [46] T. Xue, Z. Gan, S. Liao, J. Cao, Physics-embedded graph network for accelerating phase-field simulation of microstructure evolution in additive manufacturing, *npj Computational Materials* 8 (2022) 201.
- [47] C. Hu, S. Martin, R. Dingreville, Accelerating phase-field predictions via recurrent neural networks learning the microstructure evolution in latent space, *Computer Methods in Applied Mechanics and Engineering* 397 (2022) 115128.
- [48] J. Y. Choi, T. Xue, S. Liao, J. Cao, Accelerating phase-field simulation of three-dimensional microstructure evolution in laser powder bed fusion with composable machine learning predictions, *Additive Manufacturing* 79 (2024) 103938.
- [49] H. Song, L. Jiang, Q. Li, A reduced order method for Allen–Cahn equations, *Journal of computational and applied mathematics* 292 (2016) 213–229.
- [50] X. Zhou, M. Azaiez, C. Xu, Reduced-order modelling for the Allen–Cahn equation based on scalar auxiliary variable approaches, *J. Math. Study* 52 (2019) 258–276.
- [51] A. Tyrylgina, Y. Chen, M. Vasilyeva, E. T. Chung, Multiscale model reduction for the Allen–Cahn problem in perforated domains, *Journal of Computational and Applied Mathematics* 381 (2021) 113010.
- [52] Y. Lu, C. Yuan, H. Guo, Convolution tensor decomposition for efficient high-resolution solutions to the allen-cahn equation, *Computer Methods in Applied Mechanics and Engineering* 433 (2025) 117507.
- [53] J. Shen, X. Yang, Numerical approximations of allen-cahn and cahn-hilliard equations, *Discrete and Continuous Dynamical Systems - Series B* 28 (2010) 1669–1691.
- [54] S. M. Wise, C. Wang, J. S. Lowengrub, An energy-stable and convergent finite-difference scheme for the phase field crystal equation, *SIAM Journal on Numerical Analysis* 47 (2009) 2269–2288. doi:10.1137/080738143.
- [55] Z. Hu, S. M. Wise, C. Wang, J. S. Lowengrub, Stable and efficient finite-difference nonlinear-multigrid schemes for the phase field crystal equation, *Journal of Computational Physics* 228 (2009) 5323–5339. doi:10.1016/j.jcp.2009.04.020.
- [56] X. Yang, L. Ju, Efficient linear schemes with unconditional energy stability for the phase field elastic bending energy model, *Computer Methods in Applied Mechanics and Engineering* 315 (2017) 691–712. doi:10.1016/j.cma.2016.10.041.
- [57] J. Zhao, Q. Wang, X. Yang, Numerical approximations for a phase field dendritic crystal growth model based on the invariant energy quadratization approach, *International Journal for Numerical Methods in Engineering* 110 (2017) 279–300. doi:10.1002/nme.5372.
- [58] J. Shen, X. Yang, H. Yu, Efficient energy stable numerical schemes for a phase field moving contact line model, *Journal of Computational Physics* 284 (2015) 617–630. doi:10.1016/j.jcp.2014.12.046.
- [59] H. Gomez, Y. Leng, T. Hu, S. Mukherjee, V. Calo, Phase-field modeling for flow simulation, in: *Frontiers in Computational Fluid-Structure Interaction and Flow Simulation: Research from Lead Investigators Under Forty-2023*, Springer, 2023, pp. 79–117.
- [60] A. F. Chadwick, P. W. Voorhees, Recursive grain remapping scheme for phase-field models of additive manufacturing, *International Journal for Numerical Methods in Engineering* 123 (2022) 3093–3110. URL: <http://dx.doi.org/10.1002/nme.6966>. doi:10.1002/nme.6966.
- [61] T. Pinomaa, M. Lindroos, M. Walbrühl, N. Provatas, A. Laukkanen, The significance of spatial length scales and solute segregation in strengthening rapid solidification microstructures of 316L stainless steel, *Acta Materialia* 184 (2020) 1–16. doi:10.1016/j.actamat.2019.10.044.
- [62] S. M. Allen, J. W. Cahn, A microscopic theory for antiphase boundary motion and its application to antiphase domain coarsening, *Acta Metall.* 27 (1979) 1085–1095.
- [63] I. Steinbach, Phase-field models in materials science, *Modelling and Simulation in Materials Science and Engineering* 17 (2009) 073001. doi:10.1088/0965-0393/17/7/073001.
- [64] S. Wang, R. Sekerka, A. Wheeler, B. Murray, S. Coriell, R. Braun, G. McFadden, Thermodynamically-consistent phase-field models for solidification, *Physica D: Nonlinear Phenomena* 69 (1993) 189–200.
- [65] N. Moelans, A quantitative and thermodynamically consistent phase-field interpolation function for multi-phase systems, *Acta Materialia* 59 (2011) 1077–1086. doi:10.1016/j.actamat.2010.10.038.
- [66] K. Glasner, Nonlinear preconditioning for diffuse interfaces, *Journal of Computational Physics* 174 (2001) 695–711. doi:10.1006/jcph.2001.6933.
- [67] N. Moelans, B. Blanpain, P. Wollants, Quantitative analysis of grain boundary properties in a generalized phase field model for grain growth in anisotropic systems, *Physical Review B* 78 (2008) 024113. doi:10.1103/PhysRevB.78.024113.
- [68] J. Nocedal, S. J. Wright, *Numerical Optimization*, 2nd ed., Springer, New York, 2006.
- [69] D. Rosenthal, The theory of moving sources of heat and its application to metal treatments, *Transactions of the ASME* 68 (1946) 849–866.

- [70] Q. Du, V. Faber, M. Gunzburger, Centroidal voronoi tessellations: Applications and algorithms, *SIAM Review* 41 (1999) 637–676. doi:10.1137/S0036144599352836.
- [71] S. Lloyd, Least squares quantization in pcm, *IEEE Transactions on Information Theory* 28 (1982) 129–137. doi:10.1109/TIT.1982.1056489.
- [72] D. Sun, M. Asta, J. Hoyt, Crystal-melt interfacial free energies and mobilities in fcc and bcc fe, *Physical Review B* 69 (2004) 174103. doi:10.1103/PhysRevB.69.174103.
- [73] C. Kim, Thermophysical Properties of Stainless Steels, Technical Report, Argonne National Laboratory, Argonne, IL, 1975.
- [74] J. P. MacSleyne, J. P. Simmons, M. D. Graef, On the use of moment invariants for the automated analysis of 3d particle shapes, *Modelling and Simulation in Materials Science and Engineering* 16 (2008) 045008. doi:10.1088/0965-0393/16/4/045008.
- [75] D. J. Pearce, An Improved Algorithm for Finding the Strongly Connected Components of a Directed Graph, Technical Report, Victoria University of Wellington, 2005.
- [76] M. Berghaus, S. Florian, K. Solanki, C. Zinn, H. Wang, B. Butz, H. Apmann, A. von Hehl, Effect of high laser scanning speed on microstructure and mechanical properties of additively manufactured 316l, *Progress in Additive Manufacturing* 10 (2024) 1119–1132. doi:10.1007/s40964-024-00693-y.
- [77] U. S. Bertoli, B. E. MacDonald, J. M. Schoenung, Stability of cellular microstructure in laser powder bed fusion of 316l stainless steel, *Materials Science and Engineering: A* 739 (2019) 109–117. doi:10.1016/j.msea.2018.10.051.